Improving MODIS Aerosol Estimates Over Land With the Surface BRDF Reflectances Using the 3-D Discrete Cosine Transform and RossThick-LiSparse Models

Xinpeng Tian, Qiang Liu, Zhiqiang Gao, Yueqi Wang, Xiuhong Li, and Jing Wei, *Graduate Student Member, IEEE*

***Abstract*— The retrieval of aerosol properties over land from satellite sensors has always been a challenge. At present, several different algorithms for retrieving aerosol optical depth (AOD) have been developed from different satellite sensors. While each algorithm has its own advantages, the accuracy of AOD retrieval still needs to be further improved. To improve the retrieval accuracy of aerosol algorithms, it is necessary to provide a better method to describe the surface properties. In the current study, a new aerosol retrieval algorithm for Moderate Resolution Imaging Spectroradiometer (MODIS) images at a high spatial resolution of 500 m is proposed based on *a priori* bidirectional reflectance distribution function (BRDF) shape parameters database, which is reconstructed via the 3-D discrete cosine transform (DCT-PLS) method. Then, the surface reflectances are calculated from BRDF model (i.e., RossThick-LiSparse), and a non-Lambertian forward model used to describe the surface anisotropy. The new algorithm is used for processing the MODIS over the Beijing–Tianjin–Hebei of China, and Southeastern United States of America regions, and results are validated against AERONET AOD measurements as well as compared with the MODIS AOD products. The comparison showed that the estimation scheme of surface reflectance in this new algorithm significantly improved the AOD retrievals accuracy, with average correlation coefficient ∼0.965 and root-mean-square error ∼0.125; the number of AOD retrievals falling within expected error has increased to ∼80.1%, and the overestimation uncertainty has been reduced compared with MODIS products. Due to the high spatial resolution and continuous spatial distributions of the AOD retrievals by the new algorithm, therefore, it can well-captured aerosol details over mixed surfaces and better useful for air pollution studies than the MODIS products at local and urban scales.**

***Index Terms*— Aerosol optical depth (AOD), *a priori* knowledge, kernel-driven BRDF model, surface anisotropy.**

Manuscript received May 7, 2020; revised September 8, 2020 and November 24, 2020; accepted December 22, 2020.This work was supported in part by the Shandong Provincial Natural Science Foundation, China, under Grant ZR2020QD055, in part by the Key Program of Shandong Natural Science Foundation under Grant ZR2020KF031, in part by the National Natural Science Foundation of China under Grant 41876107, in part by NSFC-Shandong joint fund project under Grant U1706219, in part by the Key Research Program of Frontier Science, Chinese Academy of Sciences under Grant ZDBS-LY-7010, and in part by the National Key Research and Development Program of China under Grant 2016YFA0600102. *(Corresponding authors: Qiang Liu; Jing Wei.)*

Xinpeng Tian, Zhiqiang Gao, and Yueqi Wang are with the CAS Key Laboratory of Coastal Environmental Processes and Ecological Remediation, Yantai Institute of Coastal Zone Research, Chinese Academy of Sciences, Yantai 264003, China, also with the Shandong Key Laboratory of Coastal Environmental Processes, Yantai Institute of Coastal Zone Research, Chinese Academy of Sciences, Yantai 264003, China, and also with the Center for Mega-Science, Chinese Academy of Sciences, Qingdao 266071, China (e-mail: xptian@yic.ac.cn; zqgao@yic.ac.cn; yueqiwang@yic.ac.cn).

Qiang Liu and Xiuhong Li are with the State Key Laboratory of Remote Sensing Science, College of Global Change and Earth System Science, Beijing Normal University, Beijing 100875, China (e-mail: toliuqiang@bnu.edu.cn; lixh@bnu.edu.cn).

Jing Wei is with the Earth System Science Interdisciplinary Center, Department of Atmospheric and Oceanic Science, University of Maryland, College Park, MD 20740 USA (e-mail: weijing_rs@163.com).

Color versions of one or more figures in this article are available at https://doi.org/10.1109/TGRS.2020.3048109.

Digital Object Identifier 10.1109/TGRS.2020.3048109

I. Introduction

THE IMPACTS of atmospheric aerosols on the radiance balance of the earth are an important factor affecting global climate change [1]. Due to the complex chemical and physical properties of aerosols as well as elusive spatiotemporal variability, the uncertainty of estimating aerosol forcing is still one of the highest in climate researches [2]. They not only have some effects on climate variability by the scattering and absorption of incoming solar energy [3], but also have adverse impacts on the environment and human health [4], [5]. The aerosols are receiving increasing attention, especially in heavily polluted urban areas [6]–[8]. To improve our understanding of aerosol effects, an effective method is required to obtain the optical properties and distribution of aerosols.

Aerosol optical depth (AOD) is a crucial fundamental parameter for meteorological observation and basic optical property of aerosol derived from satellites. Over the past several decades, numerous different AOD retrieval algorithms have been proposed by using different satellite sensors [9]–[11]. The radiation signals measured by the passive satellite sensors at the top-of-the-atmosphere (TOA) contain the radiation information of both the surface and atmosphere. In general, the retrieval of atmospheric aerosols from satellite data requires separating the contribution of the surface to the satellite signals. However, satellite spectral signals do not have

enough measurement data to solve multiple unknown parameters that describe aerosol and surface properties. Therefore, the accurate reflectance properties of the surface are necessary in aerosol retrieval algorithms, and the estimation of surface reflectance is a key step in the improvement or development of retrieval algorithms over land.

Over land, the aerosol contribution in satellite signals is small compared with the surface, which makes it difficult to separate the aerosols path radiance from satellite measurements, particularly over bright urban and desert surfaces [12]. The Moderate Resolution Imaging Spectroradiometer (MODIS) aerosol products mainly include the dark target (DT) [13], [14] and deep blue (DB) [9], [15] algorithms. They use different strategies for surface reflectance estimation, while the former established hypothetical spectral relationships between the shortwave infrared and visible channels, and was mainly developed for aerosol retrieval over densely vegetated areas. In contrast, the latter built a global NDVI-dependent dynamic surface reflectance database, and was originally designed over bright surfaces. Both they provided AOD products at 10-km spatial resolutions, and DT also provided a 3-km separate product [16]. Later, Lyapustin *et al.* [10], [17] proposed a multiangle implementation of atmospheric correction (MAIAC) algorithm to retrieve AOD over land at a 1-km resolution, and has become a new operational MODIS retrieval algorithm. Recently, a high-spatial-resolution aerosol retrieval algorithm based on *a priori* land surface reflectance database (HARLS) was developed [18] over bright urban surfaces for MODIS images and then was continued to be improved (I-HARLS) on the global land [19].

However, all abovementioned DT, DB, MAIAC, HARLS, and I-HARLS algorithms are all designed based on the assumption of the Lambertian surface. In recent years, many exciting developments have taken place in improving the estimation of surface directional reflection by bidirectional reflectance distribution function (BRDF) in aerosol retrievals [20]–[23]. Almost all these retrieval methods assumed that the surface BRDF does not change during a short time period and can be obtained from existing satellite products. However, *a priori* BRDF database is directly used without further modifications which will still bring errors in aerosol retrievals [24]. Numerous studies have reported that the poor performance of current aerosol algorithms over mixed surfaces is mainly due to the problems in estimating the surface reflectance [25], [26].

Therefore, a new method is desired to reconstruct the BRDF with existing products and improve the AOD retrieval accuracy as well as the spatial resolution. For this purpose, in this article, we propose a new aerosol retrieval algorithm for MODIS images based on *a priori* BRDF shape parameters database at a 500-m resolution. This database was reconstructed by penalized least square regression based on 3-D discrete cosine transform (DCT-PLS) method [27]. Then, the bidirectional reflectance is estimated by the semiempirical kernel-driven linear BRDF model and the non-Lambert radiation transfer model. Then, the AOD retrievals are tested and validated over two typical regions with different surface and atmospheric conditions. In addition, we also compare our results with MODIS official aerosol products at different spatial resolutions.

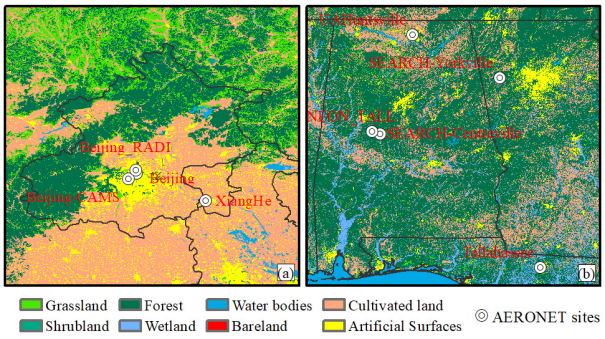

Fig. 1. Location of the AERONET stations (dots) in (a) BTH region of China and (b) SUSA.

II. Study Area and Data Sources

A. Study Region

In this study, two typical regions, i.e., the Beijing–Tianjin–Hebei (BTH) region of China and the southeastern region of the United States of America (SUSA), are selected to test and validate our algorithm (Fig. 1). These two selected regions have totally different underlying surfaces, aerosol types, aerosol loadings, and viewing angles. The former is mainly the urban surface with high brightness and dense population, where faces relatively high aerosol loadings throughout the year. In contrast, the latter is mainly the dark surface with high vegetation coverage, showing a low pollution level.

B. AERONET Data

AErosol RObotic NETwork (AERONET) is a worldwide ground-based aerosol monitoring network using CIMEL multiband sun photometers, which provides AOD measurements at multiple wavelengths with low uncertainty <0.2 every 15 min [28]. The AOD measurements have three quality levels (L), i.e., L1.0, L1.5 (cloud-screened), and L2 (cloud screened and quality-assured). The newly released Version 3 AOD measurements [29] are employed, and we prefer to use L2 data, if not available, then L1.5 data. Here, we have collected four and five AERONET sites in the BTH and SUSA regions, respectively (Fig. 1). However, it does not provide AOD measurements at 550 nm; thus, the 550-nm AODs are calculated using the Ångström exponent algorithm [30].

C. MODIS Data

Here, the Terra-MODIS MOD02HKM L1B calibrated radiance data, MOD03 geolocation data, MOD04 and MCD19A2 aerosol products, and MCD43A1 BRDF/Albedo model parameters covering two regions were collected to perform the experiment. For MODIS aerosol products, only the AOD retrievals passing the recommended quality assurance (QA) are selected for comparison. Table I shows the detailed information of ground and satellite data used in this study.

TABLE I
SUMMARY OF DATA SETS USED IN THIS STUDY

Dataset	Scientific Data Set (SDS)	Resolutions	Contents
AERONET	Aerosol optical depth	15 min	Version 3 level 1.5/2.0 AOD
MOD02HKM	EV_500_Aggr1km_RefSB	500 m, daily	Calibrated radiances
MOD03	SesorZenith, SensorAzimuth, SolarZenith, SolarAzimuth	1 km, daily	illumination geometry
MOD04_L2	Optical_Depth_ Land_And_Ocean	10 km, daily	DT AOD (QA = 3)
	Deep_Blue_Aerosol_Optical_Depth_550_Land_Best_Estimate	10 km, daily	DB AOD (QA≥ 2)
	AOD_550_Dark_Target_Deep_Blue_Combined	10 km, daily	DTB AOD (QA = 3)
MOD04_3K	Optical_Depth_ Land_And_Ocean	3 km, daily	DT AOD (QA = 3)
MCD19A2	Optical_Depth_055	1 km, daily	MAIAC AOD (QA = Best_Quality)
MOD43A1	BRDF_Albedo_Parameters_Bandx	500 m, daily	BRDF parameters (QA = 0)

III. METHODOLOGY

A. Atmospheric Radiative Transfer Model

As mentioned above, the TOA reflectance measured by satellites contains both the atmosphere and surface information. The traditional aerosol retrieval algorithm assumes that the surface is Lambertian surface, which could introduce errors into TOA reflectance simulation, and affect the accuracy of aerosol retrieval. Therefore, a fast and accurate atmospheric radiative transfer model (RTM) [31], [32] is selected to simulate TOA reflectance. It is especially suitable for describing the radiative transfer process over the non-Lambertian surface. For a given viewing geometry, the TOA reflectance ρ^{TOA} is expressed as

$$\rho^{\mathrm{TOA}}(\theta_s,\theta_v,\varphi)=\rho_0(\theta_s,\theta_v,\varphi)+\frac{T(\theta_s)R(\theta_s,\theta_v,\varphi)T(\theta_v)-t_{\mathrm{dd}}(\theta_s)t_{\mathrm{dd}}(\theta_v)|R(\theta_s,\theta_v,\varphi)|\bar{\rho}}{1-r_{\mathrm{hh}}\bar{\rho}} \quad (1)$$

where the matrices of the combinations of atmospheric transmittance $T(\theta_s)$ and $T(\theta_v)$, and the reflectance matrix $R(\theta_s,\theta_v,\varphi)$ are defined as

$$T(\theta_s)=[t_{\mathrm{dd}}(\theta_s)t_{\mathrm{dh}}(\theta_s)],\quad T(\theta_v)=[t_{\mathrm{dd}}(\theta_v)t_{\mathrm{hd}}(\theta_v)]^T \quad (2)$$

$$R(\theta_s,\theta_v,\varphi)=\begin{bmatrix} r_{\mathrm{dd}}(\theta_s,\theta_v,\varphi) & r_{\mathrm{dh}}(\theta_s,\varphi_s) \\ r_{\mathrm{hd}}(\theta_v,\varphi_v) & r_{\mathrm{hh}} \end{bmatrix}. \quad (3)$$

In the above equations, θ_s and θ_v represent the solar zenith angle (SZA) and view zenith angle (VZA), respectively, φ_s and φ_v represent solar azimuth angle and view azimuth angle, respectively, and φ is the relative azimuth angle (RAA). $|R(\theta_s,\theta_v,\varphi)|$ represents the determinant of the reflectance matrix R. Equation (1) consists of two groups of independent parameters: atmosphere- and surface-dependent parameters. The atmosphere-dependent parameters include: the path scattering reflectance $\rho_0(\theta_s,\theta_v,\varphi)$, atmospheric spherical albedo $\bar{\rho}$, the downward bidirectional path transmittances $t_{\mathrm{dd}}(\theta_s)$, directional to hemispheric path transmittance $t_{\mathrm{dh}}(\theta_s)$, the upward bidirectional path transmittances $t_{\mathrm{dd}}(\theta_v)$, and hemispheric to directional transmittance $t_{\mathrm{hd}}(\theta_v)$. The surface-dependent parameters include: the bidirectional surface reflectance $r_{\mathrm{dd}}(\theta_s,\theta_v,\varphi)$, directional to hemispheric reflectance $r_{\mathrm{dh}}(\theta_s,\varphi_s)$ (also called black-sky albedo, α_{bs}), hemispheric to directional reflectance $r_{\mathrm{hd}}(\theta_v,\varphi_v)$ [which is equal to $r_{\mathrm{dh}}(\theta_s,\varphi_s)$], and bihemispheric reflectance r_{hh} (also called white-sky albedo (WSA), α_{ws}). Subscripts d and h represent directional and hemispheric, respectively, so, the hd, hh, dh, and dd symbols stand for hemispheric-directional, bihemisphere, directional-hemispheric, and bidirectional, respectively.

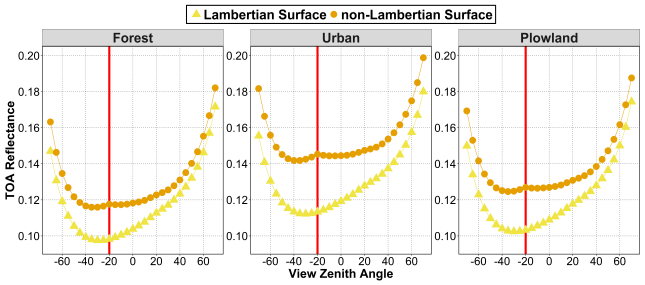

Fig. 2. Simulated reflectance at the TOA in the blue band as a function of VZA over Lambertian and non-Lambertian surfaces over various land cover types. SZA and atmospheric condition are the same in all panels ($\theta_s = 20°$, AOD = 0.1).

To expedite the calculation of the RTM model, the values of atmosphere-dependent parameters are stored in the lookup table (LUT), which is precalculated using the MODerate resolution atmospheric TRANsmission (MODTRAN) atmospheric radiative transfer code [33]. The surface-dependent parameters are calculated using the semiempirical kernel-driven BRDF model with kernel weight parameters obtained from the prebuilt BRDF database.

For Lambertian surface, the matrix R in (1) is generally expressed as a single surface reflectance (r_{hh} or r_{dd}); therefore, $|R(\theta_s,\theta_v,\varphi)|=0$. Thus, the aerosol retrieval over Lambertian surfaces is to find the result matching the LUT by comparing the simulated and satellite received TOA reflectances. Fig. 2 shows that the comparison simulated results of TOA reflectances in the blue channel as a function of VZA over Lambertian and non-Lambertian surfaces over various land cover types. There are obvious differences in TOA reflectance between above two different surfaces along with the VZA changes, and the difference increases gradually as the VZA approaches the hotspot direction, indicating that the ignorance of the surface directional reflection characteristics can increase the estimation uncertainty of aerosol retrieval, especially in the hotspot direction. More importantly, compared with forest and plowland, the difference of TOA reflectance over urban areas is much larger, which may be one of the main reasons for the poor accuracy of most current aerosol algorithms.

B. Estimation of Surface-Dependent Parameters

The angular distribution of surface reflected radiance can be described by the bidirectional reflection factor (BRF), which is the magnitude most frequently employed in radiometry. To simulate the surface anisotropy, various BRF models have been proposed, including physical [34], computer simulation [35], and empirical or semiempirical models [36], [37]. At present, the linear semiempirical kernel-driven model is the most widely used for fitting and predicting BRDF. Thus, the Ross-Thick and Li-Sparse-Reciprocal (RTLSR) kernel [38], [39] is selected to calculate the r_{dd} surface reflectance

$$r_{\mathrm{dd}}(\theta_s,\theta_v,\varphi,\lambda) = f_{\mathrm{iso}}(\lambda) + f_{\mathrm{vol}}(\lambda)K_{\mathrm{vol}}(\theta_s,\theta_v,\varphi) + f_{\mathrm{geo}}(\lambda)K_{\mathrm{geo}}(\theta_s,\theta_v,\varphi) \quad (4)$$

where λ is the wavelength; K_{vol} and K_{geo} are the volumetric and geo-optical scattering kernels, respectively; f_{iso}, f_{vol}, and f_{geo} represent the corresponding weight coefficients; K_{vol} and K_{geo} are functions of SZA, VZA, and RAA. MCD43A3 products provide the kernel weight coefficients that can be used to calculate black sky albedo with the specific illumination geometry and WSA by the following polynomial, and $g_{i,k}$ integral coefficients are provided by Lucht *et al.* [38]:

$$\begin{aligned}\alpha_{bs}(\theta,\lambda) = {} & f_{\mathrm{iso}}(\lambda)\left(g_{0,\mathrm{iso}} + g_{1,\mathrm{iso}}\theta^2 + g_{2,\mathrm{iso}}\theta^3\right) \\ & + f_{\mathrm{vol}}(\lambda)\left(g_{0,\mathrm{vol}} + g_{1,\mathrm{vol}}\theta^2 + g_{2,\mathrm{vol}}\theta^3\right) \\ & + f_{\mathrm{geo}}(\lambda)\left(g_{0,\mathrm{geo}} + g_{1,\mathrm{geo}}\theta^2 + g_{2,\mathrm{geo}}\theta^3\right). \quad (5)\end{aligned}$$

C. Reconstruction of BRDF Shape Parameters

The BRDF shape, defined by the volumetric ($V = f_{\mathrm{vol}}/f_{\mathrm{iso}}$) and the geometric ($G = f_{\mathrm{geo}}/f_{\mathrm{iso}}$) parameters, is more stable than BRDF kernel weight coefficients [39]–[41]. Thus, we assume that the BRDF shape parameters change little during a short time period. The anisotropic of the surface can be captured by the BRDF shape. MCD43A1 products can provide the three model weighting parameters. However, the estimation of these parameters is affected by errors of the atmospheric correction due to the uncertainties of atmospheric parameters or the insufficient angular range of surface reflectance data. In addition, the cloud contaminations, suboptimal illumination conditions, and errors of input surface reflectance can also cause missing data and reduce the data quality, especially over heterogeneous urban.

Here, we used the discrete cosine transform (DCT-PLS) algorithm to reduce the effects of atmospheric conditions (e.g., clouds). This method uses the strategy of minimizing the following function to find the best smoothing estimate [27].

$$F(\hat{y}) = \mathrm{wRSS} + \mathrm{sP}(\hat{y}) = \left\| W^{1/2}(\hat{y} - y) \right\|^2 + s\|D\hat{y}\|^2 \quad (6)$$

where RSS represents residual sum-of-squares, P is a penalty term, $\|\ \|$ denotes the Euclidean norm, y is a vector containing a series of BRDF shape parameters, $\hat{y}$ is the smoothed equidistant data, W is the diagonal matrix containing the weights, $w_i \in [0, 1]$ that corresponds to the data y_i, s represents a positive value that controls the smoothness of smooth data, and D is a Laplace operator.

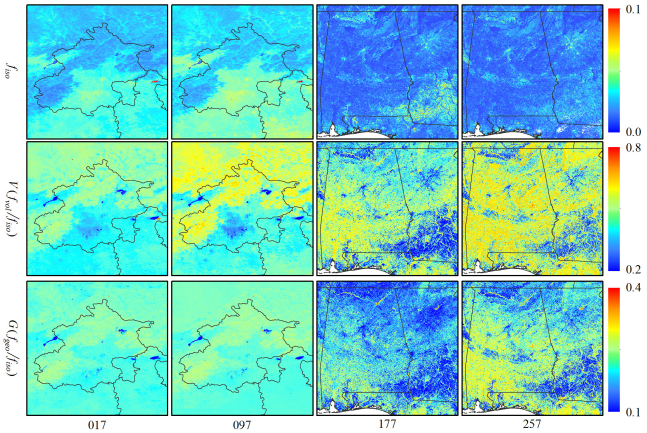

Fig. 3. Precalculated 8-day BRDF shape data set; f_{iso}, V ($f_{\mathrm{vol}}/f_{\mathrm{iso}}$) and G ($f_{\mathrm{geo}}/f_{\mathrm{iso}}$) parameters from top to bottom in the blue band on day 17, 97, 177, and 257 in the BTH region of China and the Southeastern United States of America.

The minimization of $\hat{y}$ can be achieved by iterative calculation. Through the discrete cosine transform (DCT) and inverse DCT (IDCT), the smooth output $\hat{y}$ is given by

$$\hat{y}_{\{k+1\}} = \mathrm{IDCT}\left(\Gamma\mathrm{DCT}\left(W\left(y - \hat{y}_{\{k\}}\right) + \hat{y}_{\{k\}}\right)\right) \quad (7)$$

where $y\hat{}_{\{k\}}$ is $\hat{y}$ calculated at the k-step iteration, Γ is a diagonal matrix, and its components can be expressed as

$$\Gamma_{i,j} = \left[1 + s\left(2 - 2\cos\left((i-1)\pi/n\right)\right)^2\right]^{-1} \quad (8)$$

where n is the number of elements in y. The weighting functions [42] are given by

$$w_i = \begin{cases} 1.0 & u_i > 0.0 \\ 1.0 - \left(u_i/4.685\right) & -1.0 < u_i/4.685 < 0.0 \\ 0.0 & u_i/4.685 < -1.0 \end{cases} \quad (9)$$

where u_i represents the Studentized residual, which is adjusted for leverage and standard deviation

$$u_i = r_i \left[1.4826\mathrm{MAD}(r)\sqrt{1 - \frac{\sqrt{1+\sqrt{1+16s}}}{\sqrt{2}\sqrt{1+16s}}}\right]^{-1} \quad (10)$$

where $r_i = y_i - \hat{y}_i$ denotes the residual of the ith observation, and MAD represents the median absolute deviation.

Therefore, the full-coverage eight-day BRDF shape parameters data set at a 500-m spatial resolution is reconstructed using the MCD43A1 products based on the above method for two typical regions. Fig. 3 shows some examples of the BRDF shape images on days 17, 97 in the BTH region and days 177, 257 in the SUSA region. It is clear that this data set has a high data quality that can better reflect the surface BRDF variations over both urban and vegetated areas. Due to the complex structures of urban, the f_{iso} parameter varies extensively, and it is obviously higher than those over vegetation and plowland regions. The V and R parameters appear to be larger over vegetated areas than urban areas.

D. AOD Retrieval

1) Aerosol-Type Assumption: The composition of the atmospheric aerosol changes with location and time; thus, aerosol type is another important factor in AOD retrieval. For the operational MODIS aerosol retrieval algorithms, the aerosol type is determined according to the aerosol physical and optical properties from AERONET inversions using the cluster analysis approach [14], [43]. In recent years, numerous methods to classify and characterize aerosol types have been presented. In this study, aerosol types are assumed at the seasonal level using the long-term historical ground-based observations (i.e., single scattering albedo and asymmetry factor) collected from the AERONET sites in the study regions via the time series analysis method [44].

2) Pixel Selection: The successful retrieval of aerosol algorithms is related to the effective removal of unsuitable pixels. Therefore, in this study, our proposed universal dynamic threshold cloud detection algorithm (I-UDTCDA), which has been proved to be more accurate than the MODIS official cloud algorithms, is selected to detect and mask the clouds [45]. However, different from our previous study [56], instead of the surface reflectance without considering the effects of surface directional reflections, we used r_{dd} to improve the overall accuracy of cloud detection, especially for thin clouds. In addition, snow/ice surfaces and inland water bodies are identified and masked using the normalized difference snow index (NDSI) [46] and normalized difference water index (NDWI) [47].

3) Creating the LUT With the MODTRAN: The LUTs are calculated using the MODTRAN model under the conditions of $\rho_{\mathrm{s}} = 0$ in this study. The parameter values in the simulations were set as follows: SZA (range from 0° to 80° with an interval of 5°), VZA (same as SZA), RAA (range from 0° to 180° with an interval of 10°), and AOD (0.01, 0.05, 0.1, 0.15, from 0.2 to 1.0 with an interval of 0.1, 1.2, 1.5, 2.0, and 3.0) for defined aerosol types in midlatitude summer and winter atmospheric models. Then, the aerosol retrieval is performed using the LUT approach. Fig. 4 shows the flowchart of our newly developed aerosol retrieval algorithm for MODIS images.

E. Validation Method

For validation purposes, AOD retrieval is defined by the average value of 5 × 5 pixels centered on each AERONET site [48], and to further minimize the effects of cloud contaminations. The true AOD is defined by the average value of all available AERONET AOD measurements within ±30 min of the satellite overpass times. In addition, several main statistical indicators, i.e., the number of collections (N), linear regression line, correlation coefficient (R), root mean square error (RMSE), and the MODIS expected error (EE; $\pm(0.05 + 0.15 \times \tau_{\mathrm{aer}})$, τ_{aer} is AERONET ground AOD measurements) over land [14], are selected to evaluate the AOD retrievals.

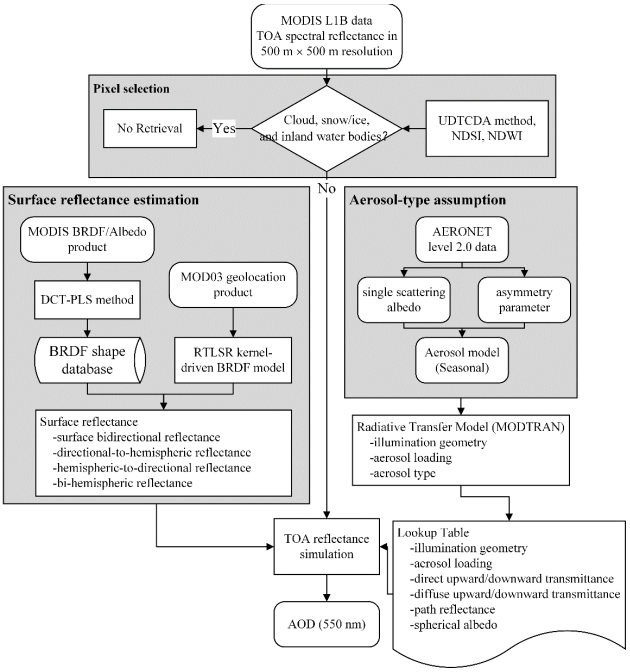

Fig. 4. Flowchart of our newly developed AOD retrieval algorithm for MODIS images over land.

IV. Results and Discussion

A. Validation of AOD Retrievals

1) Over Accuracy: Fig. 5 shows the validation and comparison of new algorithm AOD retrievals using the bihemispheric (WSA-derived) and four (as shown in (3), BRDF-derived) surface reflectances against AEROET AOD measurements in two typical regions, and over land, respectively. We have collected a total of 3523 AOD matchups in the BTH region, and the WSA-derived AOD retrievals are well correlated with the AERONET AODs ($R = 0.961$) with an RMSE of 0.168. In addition, 62.4% and 22.5% of them fall within and above the EE, indicating large overestimations. However, the overall accuracy of BRDF-derived AOD retrievals has been overall increased (e.g., $R = 0.961$, RMSE = 0.145), and the fraction within the EE ($f_{=\mathrm{EE}}$) reaches 75%, and the overestimations have been obviously decreased ($f_{>\mathrm{EE}} = 13.8\%$). In addition, similar conclusions can be obtained in the SUSA region, i.e., the BRDF-derived AOD retrievals ($N = 1401$) yield an overall higher accuracy with all improved evaluation metrics (e.g., $R = 0.923$, RMSE = 0.041, and $f_{=\mathrm{EE}} = 92.5\%$) than the WSA-derived retrievals (e.g., $R = 0.916$, RMSE = 0.052, and $f_{=\mathrm{EE}} = 86.9\%$). In general, the data quality of AOD retrievals has also been improved with an increasing R of 0.965 and $f_{=\mathrm{EE}}$ of 80.1%, and a decreasing RMSE of 0.125 using the BRDF reflectance than the WSA reflectance (i.e., $R = 0.955$, RMSE = 0.143, and $f_{=\mathrm{EE}} = 69.4\%$) over land. These results illustrate that our new algorithm improves the AOD estimates with decreasing uncertainties in different regions with varying atmospheric and surface conditions. In addition, considering the same aerosol types used, the reduced AOD overestimations

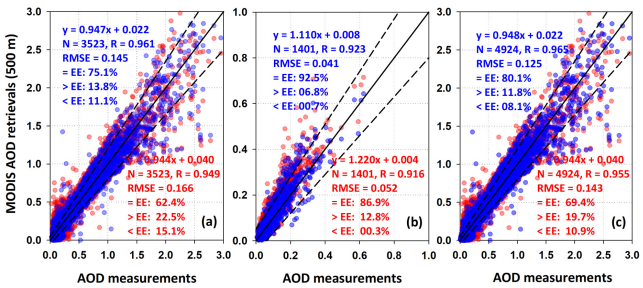

Fig. 5. Validation and comparison of WSA- (red dots) and BRDF-derived (blue dots) against AERONET AOD measurements in (a) BTH region of China, (b) Southeastern United States of America region (SUSA), and (c) over land. Black dashed and solid lines are EE lines and 1:1 line, respectively.

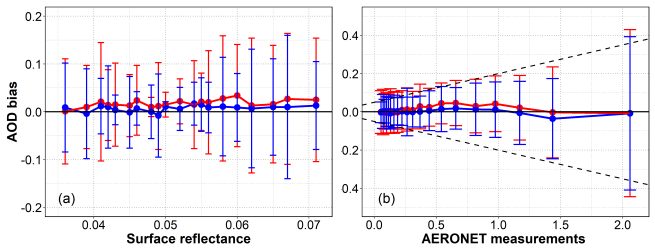

Fig. 6. AOD bias of WSA- (red dots) and BRDF-derived (blue dots) against AERONET AOD measurements AERONET AOD measurements as a function of (a) surface reflectance and (b) aerosol loadings over land. The error bars are 1 standard deviation in both directions. Zero error line is solid and EE envelopes are dashed.

are due to the improved estimates in the surface reflectance with the consideration of surface non-Lambert reflections.

2) Error Dependence: The retrieval errors related to surface reflectance and aerosol loadings are investigated (Fig. 6). For surface reflectance [Fig. 6(a)], in general, the estimate uncertainties in WSA- and BRDF-derived AOD retrievals become continuously larger with the increase of surface reflectance. The main reason is that the sensitivity of the TOA reflectance to aerosol changes decreases [19]. The mean bias of WSA-derived AOD retrievals is ∼0.018, and is larger when the surface reflectance is >0.05. In contrast, the mean biases of BRDF-derived AOD retrievals are overall lower than those of WSA-derived AOD retrievals with varying surface reflectances with a much smaller mean bias of ∼0.007. The results are expected and encouraging, i.e., the overestimations of AOD retrievals have been largely reduced, and the overall accuracy has been improved when considering the effects of surface BRDF.

For aerosol loadings [Fig. 6(b)], when AOD $\leq$ 0.5, there are overall small positive biases <0.0× of AOD retrievals using two different surface reflectance schemes. However, for high aerosol loadings (AOD > 0.5), the uncertainties of these two-scheme AOD retrievals become larger with larger standard deviations as air pollution increases. In general, the BRDF-derived AOD retrievals are overall better than the WSA-derived AOD retrievals with smaller biases closer to 0, suggesting that our revised algorithm has a better adaptability under different air pollution conditions, especially on high aerosol loadings.

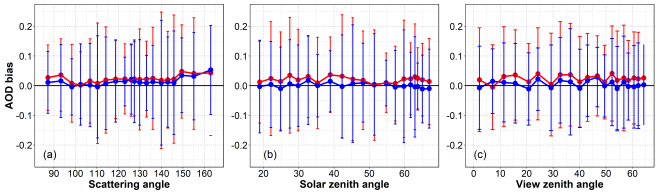

Fig. 7. AOD bias of WSA- (red dots) and BRDF-derived (blue dots) against AERONET AOD measurements as a function of (a) scattering angle, (b) SZA, and (c) VZA.

We also explored the AOD retrieval errors related to varying observation geometry conditions (Fig. 7). For scattering angles [Fig. 7(a)], the mean biases of BRDF-derived AOD retrievals are generally smaller than those of WSA-derived AOD retrievals. The scattering angle is calculated using the SZA, satellite zenith angle, and RAA. It makes the scattering angle dependence of AOD difference between retrievals and measurements difficult to interpret. Therefore, a related phenomenon is shown in Fig. 7(b) and (c), which depicts the bias as a function of the solar zenith and VZAs, respectively. In general, the biases of WSA-derived AODs are always positive with an average value of 0.020 and 0.024, while the biases of BRDF-derived AODs are much smaller and closer to 0 for two angles, respectively. These results suggest that our revised algorithm is not strongly dependent on geometric angles because, instead of isotropic Lambertian albedo, it considered the surface BRDF by calculating the reflectance from different directions, especially for the heterogeneous surfaces.

B. Comparison With Official Products

For comparison purposes, the official MODIS aerosol products, including Collection 6.1 (C6.1) 10-km DT, 3-km DT, 10-km DB, and C6 1-km MAIAC AODs, are collected for the BTH and SUSA regions, respectively.

1) Over Accuracy: First, we validated our 500-m AOD retrievals and compared it with MODIS official AOD products in the high-polluted urban area, i.e., BTH region in China (Fig. 8). Here, we have collected 985, 1672, 909, and 1476 common AOD retrievals between our and abovementioned four MODIS AOD products at different spatial resolutions in the BTH region, respectively. The 10-km DT retrievals show a poor accuracy with an average RMSE value of 0.197, and more than 46% of the retrievals falling above the EE envelope, indicating significant overestimations [Fig. 8(a)]. In addition, the 3-km DT retrievals are less accurate than the 10-km DT retrievals with only 38.1% of the retrievals falling within the EE envelope [Fig. 8(b)]. In contrast, the number of the 10-km DB data samples is approximately 1.7 times more, and the overall accuracy is much better (e.g., RMSE = 0.168, $f_{=\mathrm{EE}}$ = 63%) than the 10-km DT retrievals, and the overestimation is significantly decreased [Fig. 8(c)]. This is mainly contributed to the improved estimation model of the surface reflectance in urban areas [9]. In contrast, the 1-km MAIAC retrievals are better than both DT and DB retrievals with all improved evaluation metrics (e.g., RMSE = 0.164, $f_{=\mathrm{EE}}$ = 73%). In general, our 500-m AOD retrievals are much more accurate than the DT, DB, and MAIAC retrievals

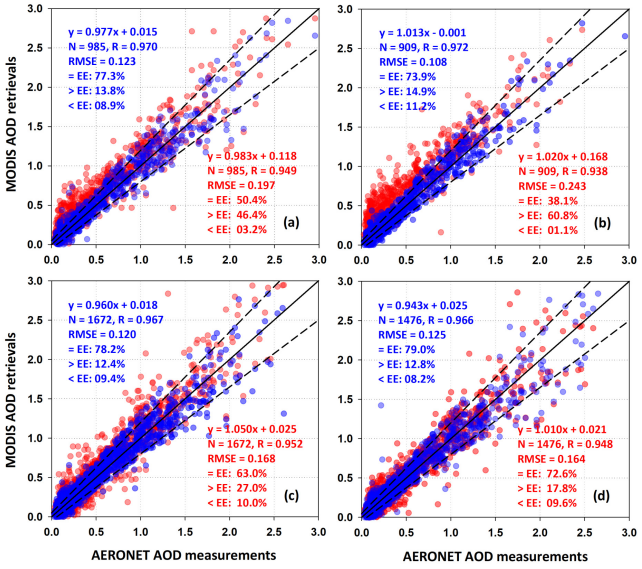

Fig. 8. Comparison of common AOD retrievals of our new AOD retrievals (500 m) with MODIS. (a) DT (10 km), (b) DT (3 km), (c) DB (10 km), and (d) MAIAC (1 km) AOD retrievals against AERONET AOD measurements in the BTH of China region. The blue and red dots represent our new AOD retrievals and the MODIS official AOD products, respectively. The black dashed and solid lines are EE lines and 1:1 line, respectively.

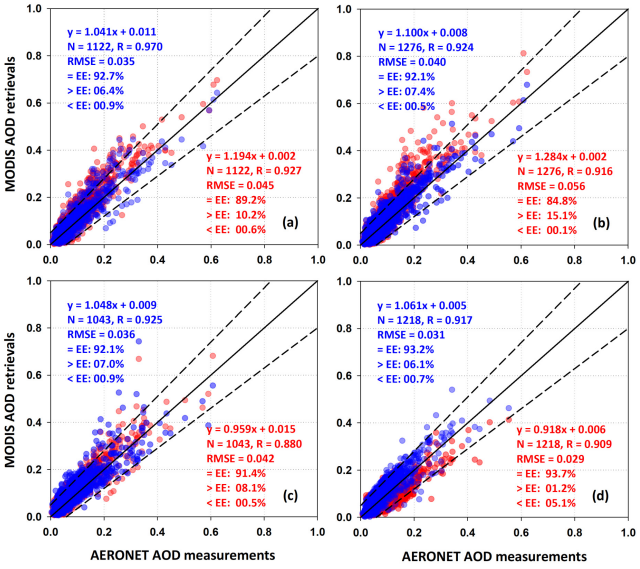

Fig. 9. Comparison of common AOD retrievals of our new AOD retrievals (500 m) with MODIS. (a) DT (10 km), (b) DT (3 km), (c) DB (10 km), and (d) MAIAC (1 km) AOD retrievals against AERONET AOD measurements in the Southeastern United States of America region (SUSA).

at coarser spatial resolutions in the BTH region where high aerosol loadings always occurred and the underlying surface is relatively bright and complex.

Then, we validated and compared our 500-m AOD retrievals with MODIS official AOD products in the clean vegetated area, i.e., SUSA region (Fig. 9). The mean measured AOD is ∼0.12, and most collected data samples range from 0 to 0.3, suggesting good air quality. There are small differences in the number of the common collocations ranging from 1043 to 1276 between different AOD products. It is clear to see that all MODIS official aerosol retrieval algorithms show similar good performance in this region with high correlations of 0.88–0.93 with ground measurements, showing small RMSE values of 0.03–0.06, and approximately 85%–94% of the retrievals fall within the EE envelopes. This is mainly because the area is typical dark surfaces which are dominated by dense vegetation, and the surface reflectance can be determined accurately. Nevertheless, there are still BRDF effects in vegetated areas that should not be ignored. Thus, after considering it, the overall accuracy of aerosol estimation has been overall improved with stronger regression lines and most evaluation metrics, especially compared with the DT and DB algorithms. These comparison results illustrate that our new algorithm also works well over vegetated areas with low aerosol loadings.

Fig. 10 shows the validation and comparison results between our AOD retrievals and different MODIS official AOD products against AERONET AOD measurements from all sites over land. We have collected a total of 2107, 2715, 2185, and 2694 common AOD retrievals between our and those MODIS AOD products abovementioned, and the number of the collocations of our new algorithm is approximately 1.8–2.3 times more than different MODIS official algorithms. In general, the DT retrievals are overall poorer with larger

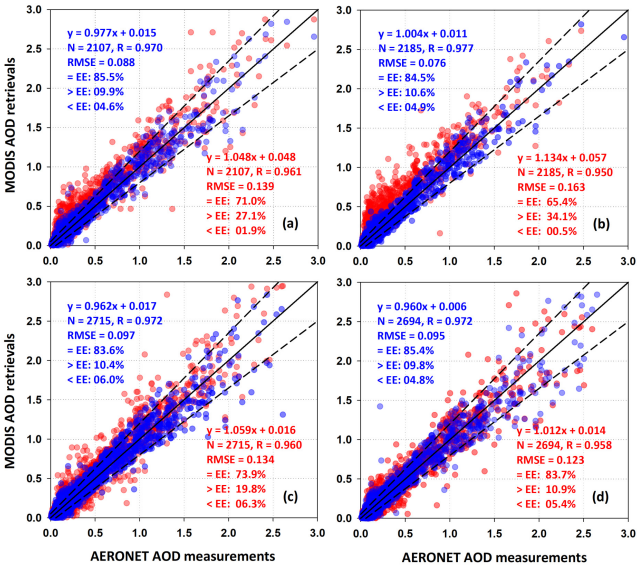

Fig. 10. Comparison of common AOD retrievals of our new AOD retrievals (500 m) with MODIS. (a) DT (10 km), (b) DT (3 km), (c) DB (10 km), and (d) MAIAC (1 km) AOD retrievals against AERONET AOD measurements in all AERONET sites over land.

uncertainties (e.g., RMSE = 0.14–0.17, $f_{>\mathrm{EE}}$ = 27%–34%) over land, and the 3-km DT AODs are generally less accurate than the 10-km DT AODs mainly due to a decrease in opportunity to discard marginal pixels from the retrieval window [49]. In contrast, the 10-km DB retrievals are better than both 10- and 3-km DT retrievals with an increasing number of the data samples, a higher $f_{=\mathrm{EE}}$ value of 74%, and a decreasing RMSE value of 0.134, because the DB algorithm allows aerosol retrieval over both dark and bright surfaces [9]. The 1-km MAIAC product yields much more data samples than the 10- and 3-km DT products but less than the 10-km DB product; in addition, it outperforms both DT and DB products with

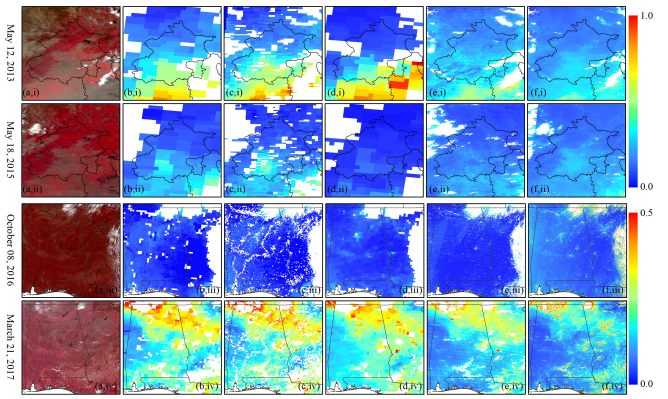

Fig. 11. Spatial distributions of (a) standard false color image (RGB = 214), (b) DT (10 km), (c) DT (3 km), (d) DB (10 km), (e) MAIAC (1 km), and (f) our new (500 m) AOD retrievals in (i) and (ii) BTH region of China and (iii) and (iv) Southeastern United States of America region (SUSA) on a low (ii) and (iii) and high (i) and (iv) aerosol loadings, respectively.

all better evaluation metrics (e.g., RMSE = 0.123, $f_{=\mathrm{EE}}$ = 83.7%). However, our 500-m AOD retrievals have the largest number of data samples and show the best accuracy with the highest $f_{=\mathrm{EE}}$ values and smallest RMSE values compared with all MODIS official AOD products over land. On the whole, the above comparison results suggest that our new algorithm works well from darkest to brightest surfaces because it not only increases the number of successful retrievals but also improves the accuracy of aerosol estimations.

2) Spatial Distributions: Last, we compared the spatial coverage and distributions under different polluted conditions among different MODIS AOD products (Fig. 11). For this purpose, four images including the high aerosol loading events on May 12, 2013 [Fig. 11(i)] and March 21, 2017 [Fig. 11(iv)], and low aerosol loading events on May 18, 2015 [Fig. 11(ii)] and October 8, 2016 [Fig. 11(iii)] over the BTH and SUSA regions, respectively. In general, our AOD product shows consistent spatial distributions with the MODIS official AOD products, e.g., high aerosol loadings appear in the urban areas of the southeastern BTH and northeastern SUSA regions, while low aerosol loadings occur in the vegetation areas of northwestern BTH and western SUSA regions. However, the 10-km [Fig. 11(c)] and 3-km DT [Fig. 11(e)] AOD products show a large number of missing values with poor spatial continuity in urban areas due to the limitations of the DT algorithm. However, the latter can provide more detailed air pollution aerosol information due to its higher spatial resolution. The DB product can retrieve AODs over bright urban areas and provides better spatial continuity than the DT algorithm [Fig. 11(d)]. Similarly, the MAIAC product allows for aerosol retrievals over the whole surface but can produce much more detailed aerosol distributions due to its 1-km higher resolution [Fig. 11(f)]. Our new algorithm can also generate AODs over both dark and bright surfaces similar to the DB and MAIAC algorithms [Fig. 11(b)]; however, it can provide a wider and more accurate spatial coverage than all the MODIS official AOD products due to our more robust cloud detection scheme. Moreover, it can also provide much more detailed AOD spatial distributions due to 2–20 times higher resolutions than all currently available MODIS official AOD products at coarser resolutions.

V. Conclusion

In this article, we have developed a new aerosol retrieval algorithm by considering the effects of surface BRDF using the RossThick-LiSparse model over land for MODIS images. Here, we assumed that the surface BRDF shapes change little during a short time period; thus, *a priori* eight-day BRDF shape data set is constructed using the MODIS BRDF/Albedo product by penalized least square regression based on 3-D discrete cosine transform (DCT-PLS) method. Then, the surface BRDF reflectances are calculated via the RossThick-LiSparse model. To test the performance of the new algorithm, two typical local regions, including the BTH region in China and the Southeastern United States of America (SUSA) region, with different underlying surfaces and aerosol loadings are selected. Then, our 500-m AOD retrievals are validated against AERONET AOD measurements in these two regions from 2013 to 2017, and also compared with MODIS official AOD products.

The results show that our AOD retrievals are highly consistent with AERONET AOD measurements, with a high correlation coefficient (R) of 0.965, a low RMSE value of 0.125, and 80.1% of the matched retrievals falling within the EE envelopes. In addition, the data quality of AOD retrievals has been largely improved compared with those without considering the effects of surface BRDF, especially over bright urban surfaces. More importantly, our AOD retrievals show a much higher spatial resolution and a superior accuracy than all current available MODIS official AOD products. These results illustrate that our new AOD product can provide wide, accurate, and detailed aerosol information, which is particularly useful for related air pollution studies in city-level areas. Nevertheless, due to the limited time and huge amount of data, we just selected two representative regions in the world for the experiment in the current study; however, we will consider extending our algorithm to the whole global scale to produce the high-resolution (500 m) and high-quality global AOD data set in our future study.

Acknowledgment

The AERONET data used in this study were available at the Goddard Space Flight Center (https://aeronet.gsfc.nasa.gov/), and the MODIS series data are available at the NASA's Earth Observing System Data and Information System (https://earthdata.nasa.gov/eosdis).

References

[1] J. H. Seinfeld *et al.*, "Improving our fundamental understanding of the role of aerosol-cloud interactions in the climate system," *Proc. Nat. Acad. Sci. USA*, vol. 113, no. 21, pp. 5781–5790, May 2016.
[2] U. Lohmann and J. Feichter, "Global indirect aerosol effects: A review," *Atmos. Chem. Phys.*, vol. 5, no. 3, pp. 715–737, Mar. 2005.
[3] V. Ramanathan *et al.*, "Warming trends in Asia amplified by brown cloud solar absorption," *Nature*, vol. 448, no. 7153, p. 575–578, Aug. 2007.
[4] J. Wei *et al.*, "Satellite-derived 1-km-resolution PM1 concentrations from 2014 to 2018 across China," *Environ. Sci. Technol.*, vol. 53, no. 22, pp. 13265–13274, Nov. 2019.

[5] J. Wei *et al.*, "Reconstructing 1-km-resolution high-quality PM2.5 data records from 2000 to 2018 in China: Spatiotemporal variations and policy implications," *Remote Sens. Environ.*, vol. 252, Jan. 2021, Art. no. 112136.

[6] X. Li, F. Wagner, W. Peng, J. Yang, and D. L. Mauzerall, "Reduction of solar photovoltaic resources due to air pollution in China," *Proc. Nat. Acad. Sci. USA*, vol. 114, no. 45, pp. 11867–11872, Nov. 2017.

[7] S. Ramachandran, "Aerosol optical depth and fine mode fraction variations deduced from Moderate Resolution Imaging Spectroradiometer (MODIS) over four urban areas in India," *J. Geophys. Res.*, vol. 112, no. D16, pp. 1–11, 2007.

[8] M. Shrivastava *et al.*, "Urban pollution greatly enhances formation of natural aerosols over the Amazon rainforest," *Nature Commun.*, vol. 10, no. 1, pp. 1–2, Mar. 2019.

[9] N. C. Hsu *et al.*, "Enhanced deep blue aerosol retrieval algorithm: The second generation," *J. Geophys. Res., Atmos.*, vol. 118, no. 16, pp. 9296–9315, Aug. 2013.

[10] A. Lyapustin *et al.*, "Multiangle implementation of atmospheric correction (MAIAC): 2. Aerosol algorithm," *J. Geophys. Res.*, vol. 116, no. D3, pp. 1–15, Feb. 2011.

[11] L. Mei, V. Rozanov, M. Vountas, J. P. Burrows, R. C. Levy, and W. Lotz, "Retrieval of aerosol optical properties using MERIS observations: Algorithm and some first results," *Remote Sens. Environ.*, vol. 197, pp. 125–140, Aug. 2017.

[12] A. A. Kokhanovsky *et al.*, "Aerosol remote sensing over land: A comparison of satellite retrievals using different algorithms and instruments," *Atmos. Res.*, vol. 85, nos. 3–4, pp. 372–394, Sep. 2007.

[13] Y. J. Kaufman, D. Tanré, L. A. Remer, E. F. Vermote, A. Chu, and B. N. Holben, "Operational remote sensing of tropospheric aerosol over land from EOS Moderate Resolution Imaging Spectroradiometer," *J. Geophys. Res., Atmos.*, vol. 102, no. D14, pp. 17051–17067, Jul. 1997.

[14] R. C. Levy *et al.*, "The collection 6 MODIS aerosol products over land and ocean," *Atmos. Meas. Techn.*, vol. 6, no. 11, pp. 2989–3034, Nov. 2013.

[15] N. C. Hsu, S.-C. Tsay, M. D. King, and J. R. Herman, "Aerosol properties over bright-reflecting source regions," *IEEE Trans. Geosci. Remote Sens.*, vol. 42, no. 3, pp. 557–569, Mar. 2004.

[16] L. A. Remer, S. Mattoo, R. C. Levy, and L. A. Munchak, "MODIS 3 km aerosol product: Algorithm and global perspective," *Atmos. Meas. Techn.*, vol. 6, no. 7, pp. 1829–1844, Jul. 2013.

[17] A. Lyapustin, Y. Wang, S. Korkin, and D. Huang, "MODIS collection 6 MAIAC algorithm," *Atmos. Meas. Techn.*, vol. 11, no. 10, pp. 5741–5765, Oct. 2018.

[18] J. Wei and L. Sun, "Comparison and evaluation of different MODIS aerosol optical depth products over the Beijing-Tianjin-Hebei region in China," *IEEE J. Sel. Topics Appl. Earth Observ. Remote Sens.*, vol. 10, no. 3, pp. 835–844, Mar. 2017.

[19] J. Wei *et al.*, "An improved high-spatial-resolution aerosol retrieval algorithm for MODIS images over land," *J. Geophys. Res., Atmos.*, vol. 123, no. 21, pp. 12291–12307, Nov. 2018.

[20] J. Wei, Z. Li, L. Sun, Y. Yang, C. Zhao, and Z. Cai, "Enhanced aerosol estimations from Suomi-NPP VIIRS images over heterogeneous surfaces," *IEEE Trans. Geosci. Remote Sens.*, vol. 57, no. 12, pp. 9534–9543, Dec. 2019.

[21] S. Shi *et al.*, "Synergy of MODIS and AATSR for better retrieval of aerosol optical depth and land surface directional reflectance," *Remote Sens. Environ.*, vol. 195, pp. 130–141, Jun. 2017.

[22] Y. Xie *et al.*, "Deriving a global and hourly data set of aerosol optical depth over land using data from four geostationary satellites: GOES-16, MSG-1, MSG-4, and Himawari-8," *IEEE Trans. Geosci. Remote Sens.*, vol. 58, no. 3, pp. 1538–1549, Mar. 2020.

[23] J. Wei, Z. Li, Y. Peng, L. Sun, and X. Yan, "A regionally robust high-spatial-resolution aerosol retrieval algorithm for MODIS images over eastern China," *IEEE Trans. Geosci. Remote Sens.*, vol. 57, no. 7, pp. 4748–4757, Jul. 2019.

[24] A. M. Sayer, G. E. Thomas, R. G. Grainger, E. Carboni, C. Poulsen, and R. Siddans, "Use of MODIS-derived surface reflectance data in the ORAC-AATSR aerosol retrieval algorithm: Impact of differences between sensor spectral response functions," *Remote Sens. Environ.*, vol. 116, pp. 177–188, Jan. 2012.

[25] X. Tian, Q. Liu, X. Li, and J. Wei, "Validation and comparison of MODIS C6.1 and C6 aerosol products over Beijing, China," *Remote Sens.*, vol. 10, no. 12, p. 2021, Dec. 2018.

[26] M. Bilal and J. E. Nichol, "Evaluation of MODIS aerosol retrieval algorithms over the Beijing-Tianjin-Hebei region during low to very high pollution events," *J. Geophys. Res., Atmos.*, vol. 120, no. 15, pp. 7941–7957, Aug. 2015.

[27] D. Garcia, "Robust smoothing of gridded data in one and higher dimensions with missing values," *Comput. Statist. Data Anal.*, vol. 54, no. 4, pp. 1167–1178, Apr. 2010.

[28] B. N. Holben *et al.*, "An emerging ground-based aerosol climatology: Aerosol optical depth from AERONET," *J. Geophys. Res., Atmos.*, vol. 106, no. D11, pp. 12067–12097, Jun. 2001.

[29] D. M. Giles *et al.*, "Advancements in the aerosol robotic network (AERONET) version 3 database—Automated near-real-time quality control algorithm with improved cloud screening for Sun photometer aerosol optical depth (AOD) measurements," *Atmos. Meas. Techn.*, vol. 12, no. 1, pp. 169–209, Jan. 2019.

[30] A. Ångström, "The parameters of atmospheric turbidity," *Tellus*, vol. 16, no. 1, pp. 64–75, 1964.

[31] W. Qin, J. R. Herman, and Z. Ahmad, "A fast, accurate algorithm to account for non-Lambertian surface effects on TOA radiance," *J. Geophys. Res., Atmos.*, vol. 106, no. D19, pp. 22671–22684, Oct. 2001.

[32] Y. Qu, S. Liang, Q. Liu, X. Li, Y. Feng, and S. Liu, "Estimating arctic sea-ice shortwave albedo from MODIS data," *Remote Sens. Environ.*, vol. 186, pp. 32–46, Dec. 2016.

[33] A. Berk and F. Hawes, "Validation of MODTRAN 6 and its line-by-line algorithm," *J. Quant. Spectrosc. Radiat. Transf.*, vol. 203, pp. 542–556, Dec. 2017.

[34] S. Jacquemoud *et al.*, "PROSPECT+SAIL models: A review of use for vegetation characterization," *Remote Sens. Environ.*, vol. 113, pp. S56–S66, Sep. 2009.

[35] J. P. Gastellu-Etchegorry, E. Martin, and F. Gascon, "DART: A 3D model for simulating satellite images and studying surface radiation budget," *Int. J. Remote Sens.*, vol. 25, no. 1, pp. 73–96, Jan. 2004.

[36] H. Rahman, B. Pinty, and M. M. Verstraete, "Coupled surface-atmosphere reflectance (CSAR) model: 2. Semiempirical surface model usable with NOAA advanced very high resolution radiometer data," *J. Geophys. Res., Atmos.*, vol. 98, no. D11, pp. 20791–20801, Nov. 1993.

[37] J.-L. Roujean, M. Leroy, and P.-Y. Deschamps, "A bidirectional reflectance model of the Earth's surface for the correction of remote sensing data," *J. Geophys. Res., Atmos.*, vol. 97, no. D18, pp. 20455–20468, 1992.

[38] W. Lucht, C. B. Schaaf, and A. H. Strahler, "An algorithm for the retrieval of albedo from space using semiempirical BRDF models," *IEEE Trans. Geosci. Remote Sens.*, vol. 38, no. 2, pp. 977–998, Mar. 2000.

[39] E. Vermote, C. O. Justice, and F.-M. Breon, "Towards a generalized approach for correction of the BRDF effect in MODIS directional reflectances," *IEEE Trans. Geosci. Remote Sens.*, vol. 47, no. 3, pp. 898–908, Mar. 2009.

[40] L. She *et al.*, "Joint retrieval of aerosol optical depth and surface reflectance over land using geostationary satellite data," *IEEE Trans. Geosci. Remote Sens.*, vol. 57, no. 3, pp. 1489–1501, Mar. 2019.

[41] X. Tian, Q. Liu, Z. Song, B. Dou, and X. Li, "Aerosol optical depth retrieval from landsat 8 OLI images over urban areas supported by MODIS BRDF/Albedo data," *IEEE Geosci. Remote Sens. Lett.*, vol. 15, no. 7, pp. 976–980, Jul. 2018.

[42] Z. Xiao, S. Liang, T. Wang, and Q. Liu, "Reconstruction of satellite-retrieved land-surface reflectance based on temporally-continuous vegetation indices," *Remote Sens.*, vol. 7, no. 8, pp. 9844–9864, Jul. 2015.

[43] A. H. Omar, "Development of global aerosol models using cluster analysis of aerosol robotic network (AERONET) measurements," *J. Geophys. Res.*, vol. 110, no. D10, pp. 1–14, 2005.

[44] J. Wei, B. Huang, L. Sun, Z. Zhang, L. Wang, and M. Bilal, "A simple and universal aerosol retrieval algorithm for Landsat series images over complex surfaces," *J. Geophys. Res. Atmos.*, vol. 122, no. 24, pp. 13338–13355, Dec. 2017.

[45] L. Sun *et al.*, "A universal dynamic threshold cloud detection algorithm (UDTCDA) supported by a prior surface reflectance database," *J. Geophys. Res., Atmos.*, vol. 121, no. 12, pp. 7172–7196, Jun. 2016.

[46] D. K. Hall, G. A. Riggs, and V. V. Salomonson, "Development of methods for mapping global snow cover using moderate resolution imaging spectroradiometer data," *Remote Sens. Environ.*, vol. 54, no. 2, pp. 127–140, Nov. 1995.

[47] B.-C. Gao, "NDWI—A normalized difference water index for remote sensing of vegetation liquid water from space," *Remote Sens. Environ.*, vol. 58, no. 3, pp. 257–266, Dec. 1996.

[48] R. C. Levy *et al.*, "Global evaluation of the collection 5 MODIS dark-target aerosol products over land," *Atmos. Chem. Phys.*, vol. 10, no. 21, pp. 10399–10420, Nov. 2010.

[49] J. Wei *et al.*, "MODIS collection 6.1 3 km resolution aerosol optical depth product: Global evaluation and uncertainty analysis," *Atmos. Environ.*, vol. 240, Nov. 2020, Art. no. 117768.

Xinpeng Tian received the B.S. degree in remote sensing science and technology and the M.S. degree in photogrammetry and remote sensing from the Shandong University of Science and Technology, Qingdao, China, in 2013 and 2016, respectively, and the Ph.D. degree in global environmental change from Beijing Normal University, Beijing, China, in 2019.

He is an Assistant Professor with the Yantai Institute of Coastal Zone Research, Chinese Academy of Sciences, Yantai, China. His main research interests focus on the radiation transfer mechanism and inversion, and aerosol retrieval from satellite data.

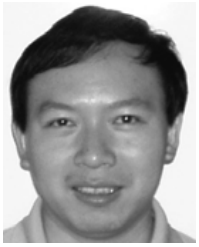

Qiang Liu received the B.S. degree in computational mathematics from Beijing University, Beijing, China, in 1997, and the Ph.D. degree in cartography and remote sensing from the Institute of Remote Sensing Applications, Chinese Academy of Sciences, Beijing, in 2002.

He is an Associate Professor with the College of Global Change and Earth System Science, Beijing Normal University, Beijing. His research interests include multiangular remote sensing, such as geometric processing of multiangular images, bidirectional reflectance distribution function (BRDF)/albedo modeling, and component temperature retrieval, as well as generation of global BRDF/albedo product.

Zhiqiang Gao received the master's degree in mapping and geographic information system from the Institute of Xinjiang Geography, Chinese Academy of Science, Xinjiang, China, in 1993, and the Ph.D. degree from the Institute of Remote Sensing Application, Chinese Academy of Science in 1998.

He is a Professor with the University of Chinese Academy of Sciences, Beijing, China, and a Research Scientist with the Yantai Institute of Coastal Zone Research, Chinese Academy of Sciences, Yantai, China. His main research interests include remote sensing application and model simulation.

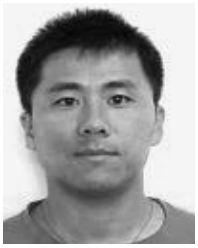

Yueqi Wang received the Ph.D. degree in environment science from the Yantai Institute of Coastal Zone Research, Chinese Academy of Sciences, Yantai, China, in 2014.

He is an Assistant Professor with the Yantai Institute of Coastal Zone Research, Chinese Academy of Sciences. His research interests include ocean color remote sensing and its environmental applications.

Xiuhong Li received the Ph.D. degree in communication and information systems engineering from Wuhan University, Wuhan, China, in 2007.

She was a Post-Doctoral Researcher with the Institute of Remote Sensing and Digital Earth, Chinese Academy of Sciences, Beijing, China, in 2008. She is an Associate Professor with the College of Global Change and Earth System Science, Beijing Normal University, Beijing. Her research interests include global changes monitoring, ground sensors networks, and ecological environmental monitoring.

Jing Wei (Graduate Student Member, IEEE) received the B.Sc. and M.S. degrees from the Shandong University of Science of Technology, Qingdao, China, in 2014 and 2017, respectively, and the Ph.D. degree from Beijing Normal University, Beijing, China, in 2020.

He conducted the joint doctoral training at the University of Maryland, College Park, MD, USA, since 2019, where he is a Post-Doctoral Fellow. He was a Research Assistant with The Chinese University of Hong Kong, Hong Kong, China, and Tsinghua University, Beijing. He has authored more than 80 articles. His research interests include satellite cloud, aerosol, fine particulate matter, and trace gas remote sensing.

Dr. Wei is a Student Member of the American Meteorological Society (AMS) and the American Geophysical Union (AGU). He is a Topic Editor of the *Big Earth Data* and a Guest Editor of the *Remote Sensing*.